Super-resolution radar imaging based on experimental OAM beams

Kang Liu, Yongqiang Cheng, Yue Gao, Xiang Li, Yuliang Qin, and Hongqiang Wang

Citation: Appl. Phys. Lett. **110**, 164102 (2017); doi: 10.1063/1.4981253
View online: http://dx.doi.org/10.1063/1.4981253
View Table of Contents: http://aip.scitation.org/toc/apl/110/16
Published by the American Institute of Physics

Super-resolution radar imaging based on experimental OAM beams

Kang Liu,[1,2,a] Yongqiang Cheng,[1] Yue Gao,[2] Xiang Li,[1] Yuliang Qin,[1] and Hongqiang Wang[1]
[1]*College of Electronic Science and Engineering, National University of Defense Technology, Changsha 410073, China*
[2]*School of Electronic Engineering and Computer Science, Queen Mary University of London, London E1 4NS, United Kingdom*

(Received 12 February 2017; accepted 6 April 2017; published online 18 April 2017)

A super-resolution imaging technique based on the vortex electromagnetic (EM) wave, which carries orbital angular momentum (OAM), is reported in this paper. The proof-of-concept experiment for the EM vortex imaging is conducted. An imaging processing method based on the real-world OAM radar data is proposed to obtain the target profile. Experimental results validate the effectiveness of the proposed imaging method and demonstrate that the vortex EM wave can be exploited to image targets with high-resolution beyond the limit of the array aperture. This breakthrough on the Rayleigh limit paves the way for innovative techniques in radar imaging and remote sensing. *Published by AIP Publishing*. [http://dx.doi.org/10.1063/1.4981253]

With additional rotational degrees of freedom generated by orbital angular momentum (OAM), OAM beams have shown practical applications in wireless communications[1–3] and radar detection realms.[4] For wireless communications, the OAM might be exploited to enhance the channel capacity and reduce the crosstalk.[1,5] In radar applications,[6,7] the OAM beams can be used to boost the target detection and imaging performance. Generally, when the conventional electromagnetic (EM) wave carries OAM, it would lead to a helical phase front, which is called "vortex electromagnetic wave."[4]

In the past three years, enormous efforts have been made to achieve high imaging resolution using the vortex EM wave. In 2013, Hu *et al.*[8] first proposed the idea that the vortex EM wave, i.e., electromagnetic vortex imaging, can be applied to image a target, which acts as a reference for the design of a new mechanism radar and the development of target recognition technology. Subsequently, Liu *et al.*[4] established theoretical imaging models based on the multiple-in-multiple-out mode and the multiple-in-single-out mode, respectively. Furthermore, concentric-ring arrays were designed and modelled to generate OAM beams for electromagnetic vortex imaging.[7,9,10] A system was proposed to generate vortex electromagnetic waves in high quality at the X-frequency band,[11] which further enhances the development of novel information-rich radar paradigm.

As aforementioned, the imaging methods, results, and conclusions on the OAM-based radar imaging are all based on the theoretical results and numerical simulations and lack experimental verification. In the open literature, only the Gaussian white noise is considered in the simulation, and the effects of the real-world background noise on the radar performance are not taken into account, which could lead to false targets in the imaging result.[7,9,10] Therefore, the existing imaging approaches would not be effective when dealing with the real-world echo reflected by targets.

In this letter, we expand the OAM-generating system in Ref. 11 to an OAM-based imaging system and carry out the proof-of-concept experiments to demonstrate the super-resolution imaging ability of the vortex EM waves. An imaging model is established according to the realistic experimental setup of our OAM-based imaging system. Furthermore, an effective imaging processing method is proposed to image the targets based on the real-world data. Finally, imaging results are obtained and imaging performance is analyzed.

Compared with traditional imaging methods, the OAM-based radar imaging technique is exploiting the approximate dual relationship between the OAM mode number (also named "topological charge") and the azimuthal angle to obtain the cross-range profile the target.[4,8] Based on the generation theory of OAM beams using a uniform circular array (UCA),[4,7] the emitted signal $s(\boldsymbol{r}, l)$ for a detection point $P(r, \theta, \phi)$ in the far-field can be given by

$$S(\boldsymbol{r}, l) = \sum_{n=1}^{N} \frac{e^{-ik|\boldsymbol{r}-\boldsymbol{q}_n|} e^{il\phi_n}}{|\boldsymbol{r}-\boldsymbol{q}_n|} \approx \frac{e^{-ikr}}{r} \sum_{n=1}^{N} e^{i(\boldsymbol{k}\cdot\boldsymbol{q}_n + l\phi_n)} \approx \frac{e^{-ikr}}{r} N i^l e^{il\phi} J_l(\mathrm{ka}\sin\theta), \quad (1)$$

where $\boldsymbol{k}$ is the wave vector, $\boldsymbol{q}_n$ is the position of the antenna element, $\phi_n = 2\pi(n-1)/N$, and $n = 1, 2, \ldots, N$ is the modulation phase for each antenna element. a denotes the array radius and $J_l(ka\sin\theta)$ is the l^{th} order Bessel function of the first kind.

According to the principle of the EM vortex imaging, an experiment is conducted in this letter based on our previous work.[11] The imaging scenario and the radar observation coordinate are illustrated in Fig. 1. In the experiments, an array radar system is exploited to generate OAM beams to illuminate the area where the targets may exist, shown in Figs. 1(a) and 2(a). The OAM-based radar system is mainly composed of a transmitting/receiving system, an antenna array, a beam control network, and a computer for data storage and signal processing.[11] As shown in Fig. 1(a), the horn antenna is used to receive the target echoes. The corner

[a]Author to whom correspondence should be addressed. Electronic mail: liukang1117@126.com

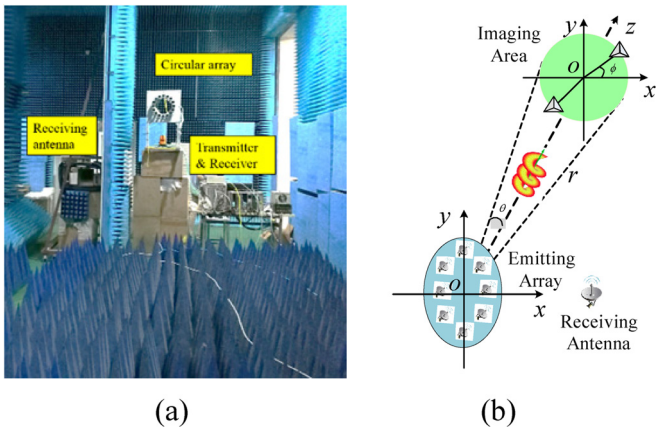

FIG. 1. Experimental setup for target imaging. (a) The imaging scenario in an anechoic chamber and (b) sketch map of the imaging observation coordinate.

reflectors are placed in the imaging scenario to be imaged, shown in Fig. 2(b). The key parameters of the experimental setup are listed in Table I. Without loss of generality, the center of the array and the center of imaging area are aligned, and the two planes are approximately parallel. According to the imaging observation coordinate shown in Fig. 1(b), the target position can be denoted by $P(r,\ \theta,\ \phi)$.

Based on the experimental setup, the received echo $S_r(\boldsymbol{r}, l)$ reflected by M scattering points can be expressed as

$$S_r(\boldsymbol{r}, l) = Ne^{il\pi/2}\sum_{m=1}^{M}\sigma_m\frac{e^{-i2kr_m}}{r_m^2}e^{il\phi_m}J_l(\mathrm{ka}\sin\theta_m) + S_{\mathrm{background}}, \tag{2}$$

where σ_m and (r_m, θ_m, ϕ_m) denote the radar cross section (RCS) and the position of the m^{th} scattering point, respectively. The background noise $S_{\mathrm{background}}$ can be given by

$$S_{\mathrm{background}} = Ne^{il\pi/2}\sum_{d=1}^{D}\sigma_d\frac{e^{-i2kr_d}}{r_d^2}e^{il\phi_d}J_l(\mathrm{ka}\sin\theta_d) + S_{\mathrm{noise}}, \tag{3}$$

which contains two parts, namely, the measurement noise S_{noise} and the echo from the object that is outside the region of interest (ROI), such as the electric wire and cable and scanning frame system in the anechoic chamber. D indicates

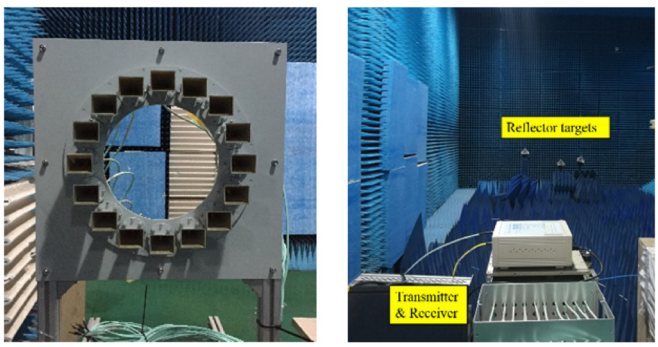

FIG. 2. Photograph of circular array and targets. (a) Circular array for OAM-generating and (b) example of target placement for imaging.

TABLE I. Key parameter setup in the experiments.

Parameter	Value
Frequency f	9.8–10 GHz
Array radius a	0.15 m
Number of antennas N	16
Topological charge l	[−7, 7]

the number of scatterers outside the ROI and the σ_d and (r_d, θ_d, ϕ_d) are the RCS and position of the d^{th} scatterer. If the background noise is not cancelled, the true target image might be interfered by the noise and false targets occur.

In the experiment, the corner reflectors are used as the targets to be detected. According to the theory of the electromagnetic vortex imaging,[4] the FFT and power spectrum density (PSD) estimation methods can be applied to process the echo reflected by the corner reflectors. However, the target profiles cannot be achieved using the imaging approaches in Refs. 4, 7, and 9 directly, due to the background noise and the phase confusion in the experiments and occurring in the real-world data. Therefore, an effective imaging processing method is proposed in Fig. 3, which mainly contains the following steps:

(1) Background noise cancellation

$$S_r(\boldsymbol{r}, l) = S_r(\boldsymbol{r}, l) - S_0(\boldsymbol{r}, l), \tag{4}$$

where $S_0(\boldsymbol{r}, l)$ indicates the echo from the background when there exist no targets, which might contain false targets.

(2) Phase compensation

$$S_r(\boldsymbol{r}, l) = S_r(\boldsymbol{r}, l) \times \exp(i\Phi), \tag{5}$$

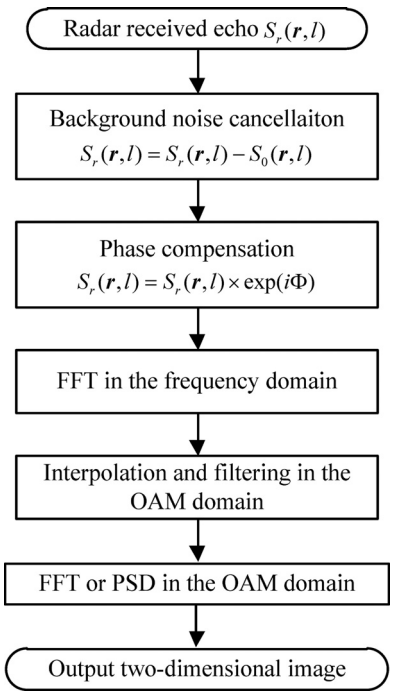

FIG. 3. The flow chart of the proposed imaging process for experimental data.

where $\Phi = \pi$ when $J_l(\mathrm{ka}\sin\theta_m) < 0$; else $\Phi = 0$. For the Bessel function $J_l(\mathrm{ka}\sin\theta_m)$, l is dependent on the emitted OAM beams, a denotes the array radius, and $k = 2\pi f_0/c$ is the wave number (f_0 is the center frequency of the signal and c is the light speed in the vacuum). θ_m can usually be set as the main-lobe direction of the radiation pattern,[10] which is decided by the OAM mode number l and the array radius a.

(3) Interpolation and filtering
The interpolation on the topological charge domain is performed first and then a Taylor Window is added to suppress the side lobes.

(4) FFT or PSD estimation
The fast Fourier transform and the power spectrum density estimation are conducted on the echo to obtain the image of the targets.

For FFT or Periodogram methods,[4] the signal reconstruction performance is independent of the number of signals, so it can be seen that the target complexity has only little influence on the imaging performance, which will be illustrated by experimental results. According to the imaging model and the signal processing method introduced above, the imaging results of the real-world experimental data are presented and analyzed. First, two corner reflectors are placed at two positions with different ranges and different azimuthal angles, i.e., $P_1(7\,m,\ 11^\circ, \pi)$ and $P_2(8\,m,\ 11^\circ, 0.8\pi)$. According to the existing imaging methods in open literatures,[4,7] the results are shown in Figs. 4(a) and 4(b). In contrast, the imaging results using the proposed methods in this letter are shown in Figs. 4(c) and 4(d). It can be seen from Figs. 4(c) and 4(d) that two targets occur at the positions $(6.92\,\mathrm{m},\ 11^\circ,\ 1.02\pi)$ and $(7.95\,\mathrm{m},\ 11^\circ,\ 0.76\pi)$, respectively, which demonstrates the effectiveness of the proposed imaging method. Moreover, compared with the image obtained by the FFT method, the imaging results based on the Periodogram method has much lower side lobes.

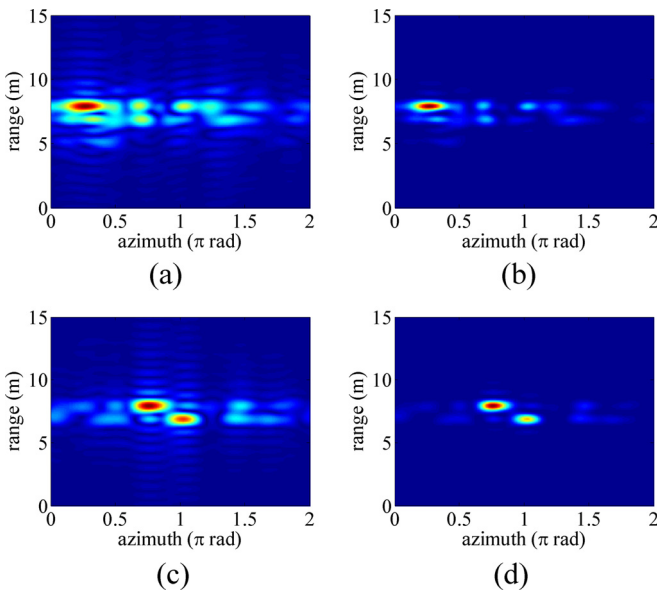

FIG. 4. Electromagnetic vortex imaging results of two reflectors. (a) The existing method in open literatures (FFT), (b) the existing method in open literatures (Periodogram), (c) the proposed method (FFT), and (d) the proposed method (Periodogram).

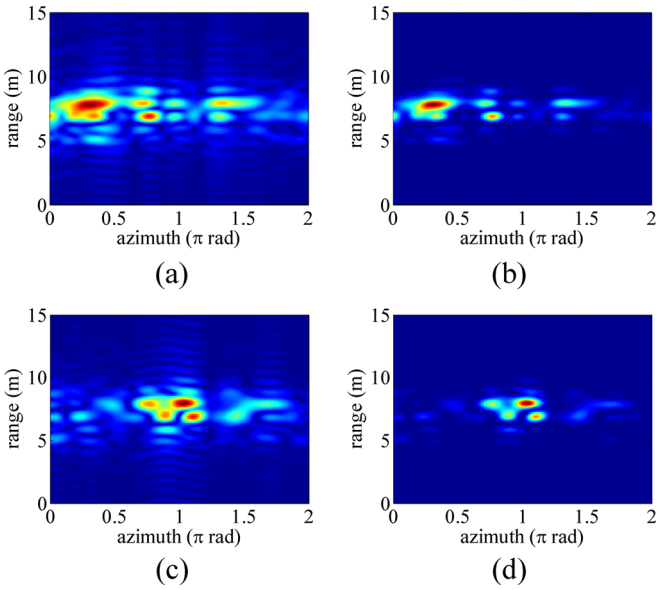

FIG. 5. Electromagnetic vortex imaging results of four reflectors. (a) The existing method in open literatures (FFT), (b) the existing method in open literatures (Periodogram), (c) the proposed method (FFT), and (d) the proposed method (Periodogram).

To further validate the proposed imaging processing method, four corner reflectors are also imaged and the results are shown in Fig. 5. The coordinates of the four reflectors are set as $P_1(7\,m,\ 11^\circ, 0.9\pi)$, $P_2(7\,m,\ 11^\circ, 1.1\pi)$, $P_3(8\,m,\ 11^\circ, 0.8\pi)$, and $P_4(8\,m,\ 11^\circ, \pi)$. As expected, four points occur at the positions $(7\,m,\ 11^\circ, 0.89\pi)$, $(7\,m,\ 11^\circ, 1.08\pi)$, $(7.95\,m,\ 11^\circ, 0.77\pi)$, and $(7.95\,m,\ 11^\circ, 0.98\pi)$.

To illustrate the super-resolution imaging ability of the vortex EM wave, more imaging experiments are performed, and the comparisons of imaging results of the traditional array imaging (real aperture imaging) and the EM vortex

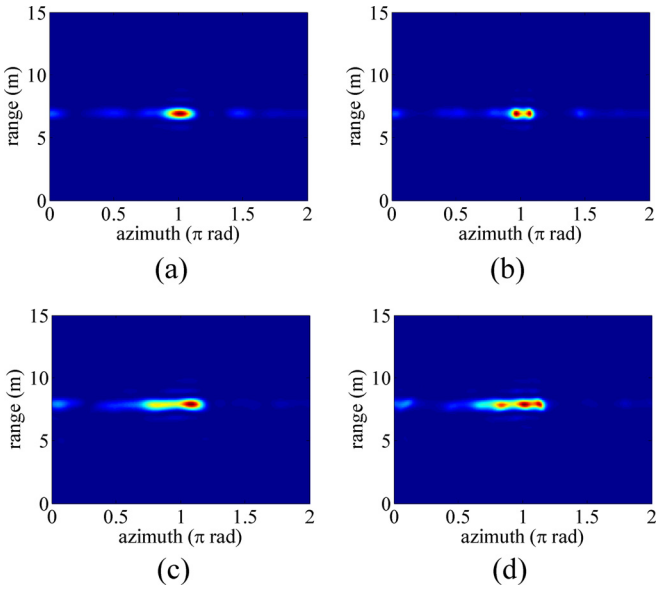

FIG. 6. Comparisons of imaging results between the traditional array imaging and the electromagnetic vortex imaging. (a) Traditional array imaging of two reflectors, (b) electromagnetic vortex imaging of two reflectors, (c) traditional array imaging of three reflectors, and (d) electromagnetic vortex imaging of three reflectors.

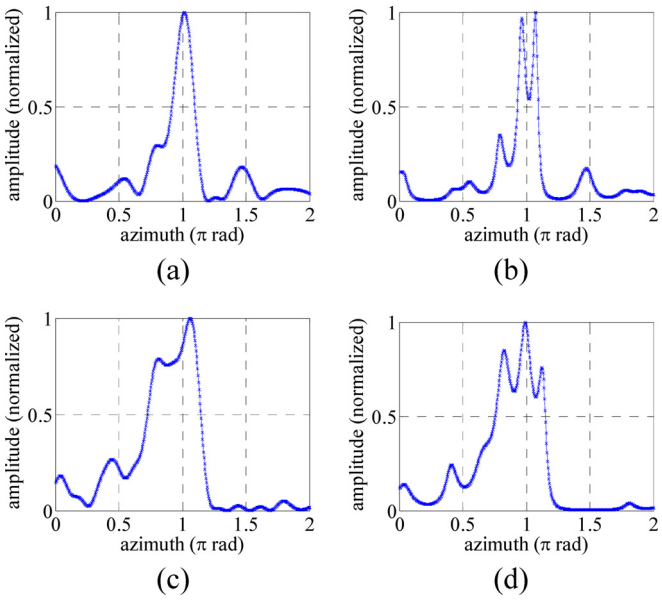

FIG. 7. Azimuthal profiles of the targets. (a) Traditional array imaging of two reflectors, (b) electromagnetic vortex imaging of two reflectors, (c) traditional array imaging of three reflectors, and (d) electromagnetic vortex imaging of three reflectors.

imaging are shown in Fig. 6. The corresponding azimuthal profiles are depicted in Fig. 7.

In Figs. 6(a) and 6(b), two reflectors are placed at the positions $P_1(7\,m,\ 10^\circ, \pi)$ and $P_2(7\,m,\ 10^\circ, 1.1\pi)$. The results demonstrate that the cross-range resolution of the traditional array imaging is 0.8 m, whereas the resolution of the EM vortex imaging is 0.39 m. As shown in Figs. 7(a) and 7(b), two reflectors can be distinguished when the targets are illuminated by the vortex EM wave. Furthermore, three reflectors are also imaged and the results are shown in Figs. 6(c) and 6(d). The positions of the three reflectors are set as

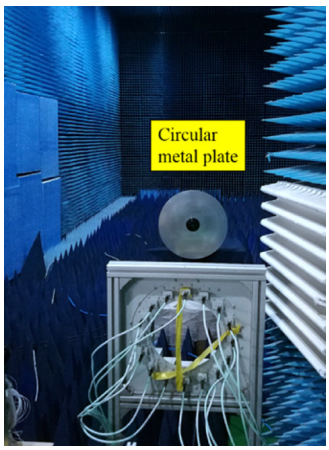

FIG. 8. Photograph of imaging scenario of the circular metal plate.

$P_1(8\,m,\ 9^\circ, 0.8\pi)$, $P_2(8\,m,\ 9^\circ, \pi)$, and $P_3(8\,m,\ 9^\circ, 1.1\pi)$. It is clear from the results that the three targets cannot be recognized when using the traditional array imaging technique, while the imaging resolution can be improved using the vortex EM wave, displayed in Figs. 7(c) and 7(d). Based on Eq. (2) and the imaging results, the cross-range resolution ρ_a for the electromagnetic vortex imaging takes the form

$$\rho_a = R \sin\theta' \times \pi/\Delta l, \tag{6}$$

where Δl is the range of OAM modes exploited in the imaging. R and θ' denote the distance from the target to the radar and the elevation angle of the target, respectively. Due to the fact that the resolutions of the range profile for both traditional array imaging and electromagnetic vortex imaging are decided by the signal bandwidth,[7] the imaging resolution in the range domain is 0.75 m ($c/2B$, where c denotes the light speed in the vacuum and B signifies the signal bandwidth).

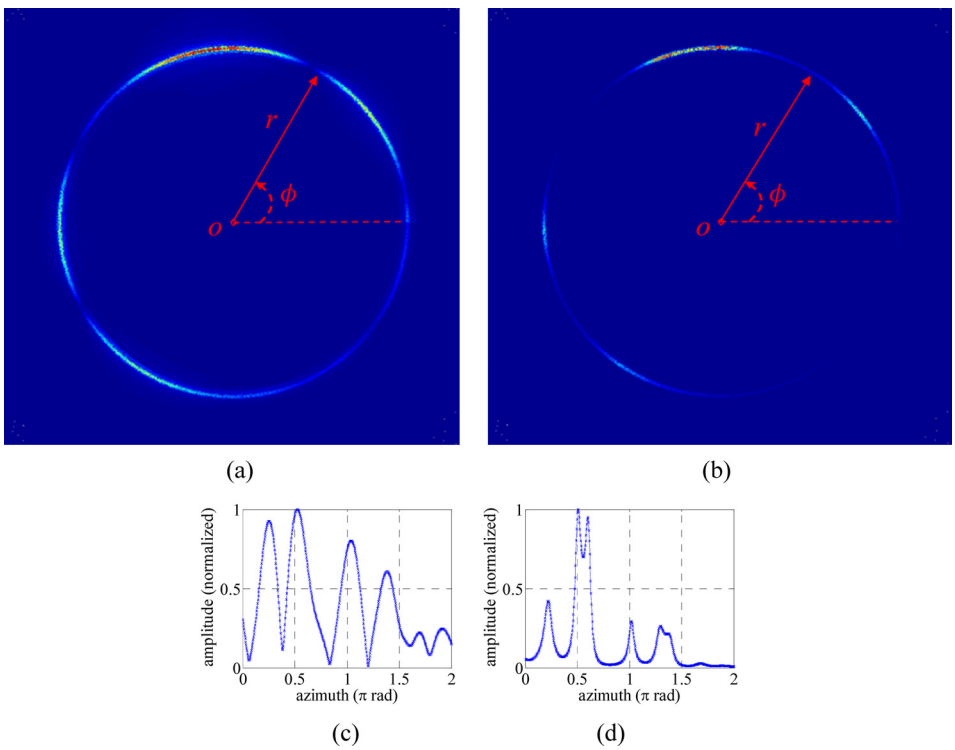

FIG. 9. Imaging results of circular metal plate. (a) 2-D profile using traditional array imaging, (b) 2-D profile using electromagnetic vortex imaging, (c) azimuthal profile using traditional array imaging, and (d) azimuthal profile using electromagnetic vortex imaging.

To further validate the high-resolution imaging ability of the proposed method, an imaging experiment of the circular metal plate is conducted. As shown in Fig. 8, the OAM-based radar transmits OAM beams to illuminate the circular plate. In the experiment, the distance between the circular plate and the transmitting array is 2.1 m, and the radius of the metal plate is 0.25 m. According to the imaging observation coordinate shown in Fig. 1(b), we can find that the distance r from each point on the circular plate to the coordinate origin is almost the same. Hence, the obtained target profile is a ring in the polar coordinate $r - o - \phi$, shown in Fig. 9. The results indicate that a ring profile occurs at the distance $r \approx 2.12$ m. Compared with traditional array imaging, the electromagnetic vortex imaging can achieve higher resolution in the azimuthal profile.

In summary, a proof-of-concept experiment has been conducted to validate the super-resolution imaging ability of vortex electromagnetic waves. The imaging model was derived and an imaging processing method was proposed, which has taken into account the effects of the background noise and phase confusion in the experiment. Experimental results demonstrated the effectiveness of the proposed imaging method and showed that the OAM-based imaging technique can improve the cross-range resolution 2 times than that of the traditional array imaging.

In future, it calls for more work on the OAM-based imaging system design and the theoretical and experimental demonstration of the upper bound of the imaging resolution improvement.

This work was supported by the National Natural Science Foundation of China under Grant No. 61302149 and by the National Natural Science Foundation of China under Grant No. 61571011.

[1]F. Tamburini, E. Mari, A. Sponselli, B. Thidé, A. Bianchini, and F. Romanato, New J. Phys. **14**, 033001 (2012).
[2]S. X. Yu, L. Li, G. M. Shi, C. Zhu, and Y. Shi, Appl. Phys. Lett. **108**, 241901 (2016).
[3]S. X. Yu, L. Li, G. M. Shi, C. Zhu, X. X. Zhou, and Y. Shi, Appl. Phys. Lett. **108**, 121903 (2016).
[4]K. Liu, Y. Q. Cheng, Z. C. Yang, H. Q. Wang, Y. L. Qin, and X. Li, IEEE Antennas Wireless Propag. Lett. **14**, 711 (2015).
[5]X. Chen, S. L. Zheng, W. T. Zhang, Y. L. Chen, H. Chi, X. F. Jin, and X. M. Zhang, IEEE Microwave Wireless Compon. Lett. **26**, 738 (2016).
[6]M. T. Lin, Y. Gao, P. G. Liu, and J. B. Liu, IET Electron. Lett. **52**, 1168 (2016).
[7]K. Liu, Y. Q. Cheng, X. Li, H. Q. Wang, Y. L. Qin, and Y. W. Jiang, IET Microwave Antennas Propag. **10**, 961 (2016).
[8]G. R. Guo, W. D. Hu, and X. Y. Du, J. Natl. Univ. Def. Technol. **35**, 71 (2013).
[9]T. Z. Yuan, H. Q. Wang, Y. L. Qin, and Y. Q. Cheng, IEEE Antennas Wireless Propag. Lett. **15**, 1024 (2016).
[10]K. Liu, Y. Q. Cheng, X. Li, Y. L. Qin, H. Q. Wang, and Y. W. Jiang, IEEE Antennas Wireless Propag. Lett. **15**, 1873 (2016).
[11]K. Liu, H. Y. Liu, Y. L. Qin, Y. Q. Cheng, S. N. Wang, X. Li, and H. Q. Wang, IEEE Trans. Antennas Propag. **64**, 3850 (2016).